Polymer 53 (2012) 5437–5448

Contents lists available at SciVerse ScienceDirect

Polymer

journal homepage: www.elsevier.com/locate/polymer

Feature article

Toward high performance inverted polymer solar cells

Xiong Gong

Department of Polymer Engineering, College of Polymer Science and Polymer Engineering, The University of Akron, Akron, OH 44325, USA

ARTICLE INFO

Article history:
Received 1 August 2012
Received in revised form
6 September 2012
Accepted 10 September 2012
Available online 17 September 2012

Keywords:
Photovoltaic devices
Inverted device structure
High performance

ABSTRACT

Bulk heterojunction (BHJ) polymer solar cells (PSCs) that can be fabricated by solution processing techniques are under intense investigation in both academic institutions and industrial companies because of their potential to enable mass production of flexible and cost-effective alternative to silicon-based solar cells. A combination of novel polymer development, nanoscale morphology control and processing optimization has led to over 8% of power conversion efficiencies (PCEs) for BHJ PSCs with a conventional device structure. Attempts to develop PSCs with an inverted device structure as required for achieving high PCEs and good stability have, however, met with limited success. Here, we report that (1) solution-processed zinc oxide (ZnO) thin film as an electron extraction layer for inverted polymer solar cells. Operated at room temperature, no obviously degradation was observed from the PSCs with ZnO layer after continuously illuminating the devices for 4 h. However, a significantly degradation was observed from the PSCs without ZnO buffer layer after illuminating the devices only for 1 h. Furthermore, PSCs with ZnO buffer layer also show very good shelf stability; only 10% degradation observed in PCEs after 6 months; (2) a high PCE of 8.4% under AM 1.5G irradiation was achieved for BHJ PSCs with an inverted device structure. This high efficiency was obtained through interfacial engineering of solution-processed electron extraction layer, ZnO, leading to facilitate electron transport and suppress bimolecular recombination. All these results provided an important progress for solution-processed PSCs, and demonstrated that PSCs with an inverted device structure are comparable with PSCs with the conventional device structure.

1. Introduction

Bulk heterojunction (BHJ) polymer solar cells (PSCs) based on polymer-fullerene composites are of growing interest as potential sources of renewable and clean energy due to their attractive advantages of low cost fabrication in large areas and light weight on flexible substrates [1–7]. Despite over 8% power conversion efficiency (PCE) reported for BHJ PSCs with a conventional device configuration of ITO/PEDOT:PSS/BHJ composite/Ba(Al), where ITO is indium tin oxide; PEDOT:PSS is poly(ethylenedioxythiophene):polystyrene sulphonate, Ba is Barium and Al is Aluminum [8–11], one finds that PEDOT:PSS on ITO are unstable with indium contaminating the polymer and thus degrading the performance of PSCs [12,13]; meanwhile, Ba/Al is inherently flawed in lower long-term stability [14,15]. In contrast, inverted PSCs were developed. In where, air-stable high-work-function metals, typically, Ag or Au, used as the anode, ITO used as the cathode. Therefore, the elimination of the PEDOT:PSS layer improves PSCs stability [16–21]. Moreover, in the inverted PSCs, the anode, such as Ag (or Au), which can be formed using coating or printing technology from Ag (or Au) pastes, to simplify and lower the cost of manufacturing [22].

In the inverted PSCs, the challenge to reverse the layer sequence of PSCs is to prepare a selective contact bottom cathode [23]. n-type metal oxide such as titanium oxide (TiO_x), zinc oxide (ZnO), cesium carbonate (Cs_2CO_3) and others used to modify cathode electrode. For example, titanium oxide (TiO_x), as an electron-transporting, a hole-blocking layer [24] and an optical spacer, was also used for modification of the surface between organic layer and ITO cathode [25–27]. All these studies indicated that the performance of inverted PSCs is sensitive to the interface between ITO cathode and the active layer. Due to the organic/ITO interface modified by introduction of buffer layer, inverted PSCs with PCEs ranging from 3% to 7% were reported [28–33]. However, the PCEs observed from PSCs with the inverted device structure are still not comparable with those obtained from PSCs with the conventional device configuration [34,35]. Therefore, the need to improve the PCEs requires the implementation of new materials and exploration of new device structures.

Recently, ZnO has drawn much attention because it has a good transparency in whole visible region and a good electron mobility

E-mail address: xgong@uakron.edu.

0032-3861/$ – see front matter © 2012 Elsevier Ltd. All rights reserved.
http://dx.doi.org/10.1016/j.polymer.2012.09.023

[36–38]. Moreover, ZnO thin film can be easily deposited from corresponding solution via various solution processes following thermal annealing treatment. All these features make ZnO an ideal material as a buffer layer for PSCs with an inverted device structure [18,39].

Here we summarize the strategies we have developed to approach high performance inverted polymer solar cells. In section II, we report solution-processed ZnO thin film as an electron extraction layer for inverted polymer solar cells. Operated at room temperature, no obviously degradation was observed from the PSCs with ZnO layer after continuously illuminating the devices for 4 h. However, a significantly degradation was observed from the PSCs without ZnO buffer layer after illuminating the devices only for 1 h. Furthermore, PSCs with ZnO buffer layer also show very good shelf stability; only 10% degradation observed in PCEs after 6 months. In section III, we report high performance BHJ PSCs with an inverted structure. By casting a thin conjugated polyelectrolyte layer onto the solution-processed ZnO thin film, the interface between ZnO electron extraction layer and BHJ active layer is re-engineered, as a result, a record PCE of 8.4% under AM 1.5 G irradiation is achieved for BHJ PSCs with the inverted structure. All these results demonstrate that electron extraction layer plays an important role in enhancement of PSCs performance with an inverted device structure.

2. Solution-processed ZnO thin film as an electron extraction layer for inverted polymer solar cells

2.1. ZnO thin film

2.1.1. Preparation

ZnO thin films coated on top of ITO glass were obtained from solution by sol–gel method. Before coating ZnO thin films, the ITO glass substrates were cleaned by ultrasonic treatment in acetone, detergent, deionized water and isopropyl alcohol sequentially. ZnO precursor was prepared by dissolving zinc acetate (ZnAc: Sigma–Aldrich) and ethanolamine in the solution of 2-methoxyethanol with a concentration of 0.5 $molL^{-1}$. Approximately 40 nm ZnO thin films were obtained by spin-casting above solution following annealed at 200 °C for 10 min. Then the thin films were continuously annealed in air at 200 °C for 1 h. Note that the ZnO precursor was not heated gradually from room temperature to the temperature being treated [37]. ZnO thin films were then ultrasonicated in acetone and isopropyl alcohol, and subsequently dried in an oven for fabrication PSCs.

2.1.2. Characterization

2.1.2.1. Absorption spectra. The absorption spectrum of ZnO thin film was measured by an HP 8453 UV–vis spectrophotometer. Fig. 1 shows the absorption spectrum of ZnO thin film thermally annealed at 200 °C. ZnO thin films are transparency from 400 nm to 1000 nm. This indicated that ZnO thin films only block the light with wavelength shorter than 400 nm.

2.1.2.2. X-ray diffraction patterns. The ZnO thin films for x-ray diffraction (XRD) patterns were obtained by spin-coating the ZnO precursor on top of the SiO_2 substrate following thermal annealing at temperature of 200 °C and 500 °C, respectively. Fig. 2 shows the XRD patterns of ZnO thin films annealed at 200 °C and 500 °C for 1 h. No diffraction peaks were observed from this pattern. To confirm the structure of the ZnO thin film, the XRD patterns of ZnO thin films annealed at 500 °C for 1 h was also shown in Fig. 2. Three peaks located at 31.7°, 34.4°, and 36.3° were observed. These indicated that the ZnO thin film annealed at 500 °C formed a polycrystalline structure.

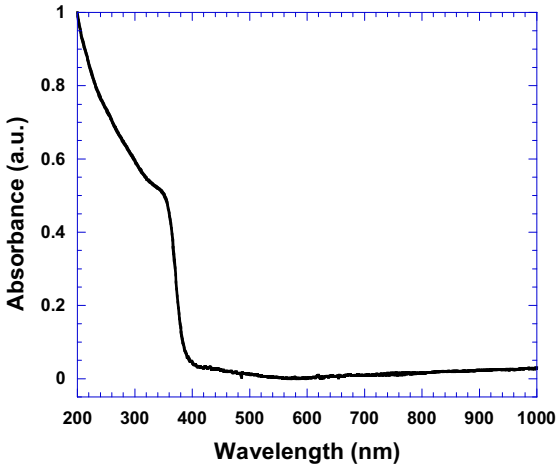

Fig. 1. Absorption spectrum of ZnO thin film.

2.1.2.3. XPS and UPS spectra. x-photoelectron spectroscopy (XPS) was performed by an ESCALAB 250 XPS instrument with Al Kα line at 1486.6 eV as the X-ray radiation source and the energy resolution was 0.1 eV. All XPS spectra were firstly calibrated by the C 1s peak (284.8 eV) from contamination to compensate the charge effect. Voigt (mixed Lorentzian–Gaussian) line shapes are used to fit all peaks. Fig. 3a shows the whole spectra of the ZnO, in which zinc, oxygen and carbon element were recorded. The peak located at 1021.50 eV in the core-level spectrum of Zn $2p_{3/2}$ state recorded from the ZnO sample has a quite symmetric shape, as shown in Fig. 3b. This indicated that a uniform bonding state corresponding to the Zn–O bond was formed.

In the core-level spectrum of O 1s state, as shown in Fig. 4a, a peak located at 531.73 eV was also observed. This peak is slightly different to the peak of O 1s located at 530.4 eV. 18.56% atomicity of O 1s is mismatched with 41.08% of Zn $2p_{3/2}$. This implies that the possibility for the formation of oxygen vacancies were took place near the ZnO surface. The positions of inelastic cutoff and valence band edge were located at 6.21 and 19.78 eV, respectively. These were determined by linear extrapolation of the leading edge to the extended base line of the ultraviolet photoelectron spectroscopy (UPS) spectra which was shown in Fig. 4b. The valence level of sample can be calculated by this equation:

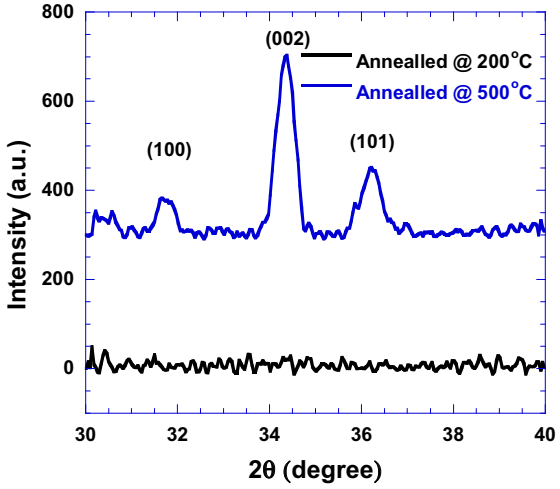

Fig. 2. XRD pattern of the solution-processed ZnO thin film annealed at 200 °C and 500 °C, respectively.

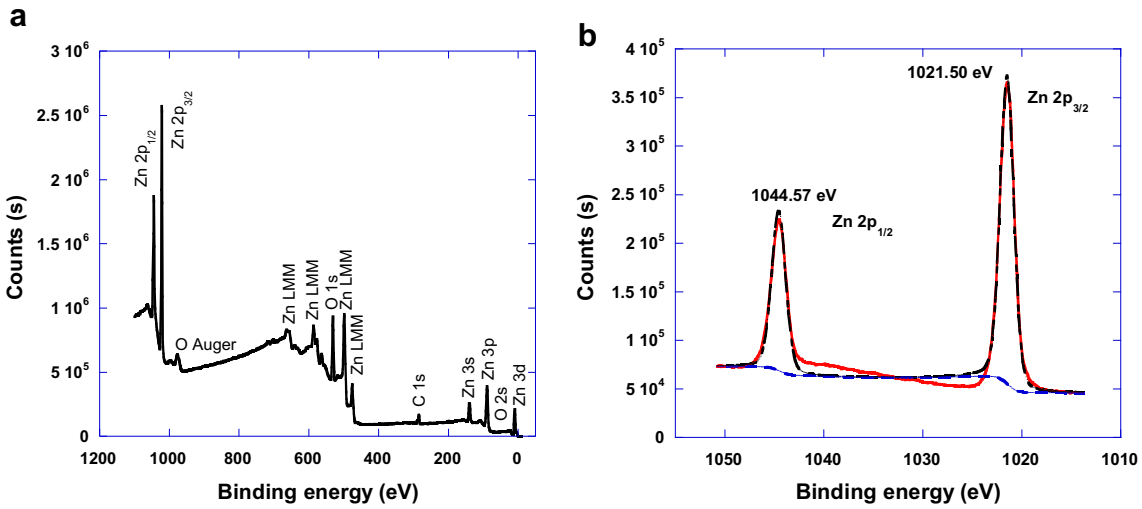

Fig. 3. a) XPS of the ZnO thin film; b) Zn 2p core-level spectra of the ZnO.

$$\mathrm{hv} - E_v = E_{\mathrm{vbe}} - E_{\mathrm{cutoff}} \quad (1)$$

where hv is the energy of photoelectron, E_v is the position of valence band of sample, E_{vbe} is valence-band edge, and E_{cutoff} is inelastic cutoff. The energy position of valence-band relative to vacuum energy is −7.61 eV. The absorption edge of ZnO was located at 390 nm, which was observed from its absorption spectrum. The optical bandgap of ZnO is − 3.19 eV. Therefore, the conduction band of ZnO is −4.42 eV.

2.1.2.4. AFM images. Tapping-mode atomic force microscopy (AFM) images were obtained using a NanoScope NS3A system (Digital Instrument) to observe the surface morphology of ZnO. Fig. 5 shows the surface roughness of ZnO thin film thermally annealed at 200 °C. The surface roughness of ZnO thin films is 1.32 nm. Such smooth surface allows high quality polymer films to be fabricated onto the top of ZnO thin films.

2.1.2.5. TEM images. The bright field (BF) transmission electron microscopy (TEM) images of the ZnO thin film annealed at 200 °C is shown in Fig. 6. Three diffraction rings were observed which indicates that the ZnO thin film forms a polycrystalline structure even though the annealing temperature is as low as at 200 °C. The BF image shows that the ZnO thin film is quite uniform. Many nanoscale fibrils with a diameter of ~10 nm were observed. No visible pinhole was observed in this BF TEM image. This indicated that the ZnO thin film was quite dense.

2.1.2.6. Electron mobility. in order to investigate the electron transporting properties of ZnO thin film, we have fabricated ZnO filed-effect transistors (FETs). Fig. 7a shows the FETs device structure. The current–voltage characteristics of ZnO FETs are shown in Fig. 7b. Electron mobility, μ, was extracted from the linear regime of transfer characteristics, using

$$\mu = (2L/WC_i)\left[I_{\mathrm{ds}}^{1/2}/(V_g - V_{\mathrm{th}})\right]^2 \quad (2)$$

where W and L are the channel width and length, respectively. C_i is the silicon dioxide gate capacitance (which is 1.0×10^{-9} F cm^{-2} for a gate oxide thickness of 300 nm). V_{th} is threshold voltage. I_{ds}, V_{ds}, and V_g are source-drain current, source-drain voltage and gate voltage, respectively. From the I_{ds}–V_g curves, the electron mobility in the saturation regime was found to be 4.46×10^{-4} cm^2 V^{-1} s^{-1}

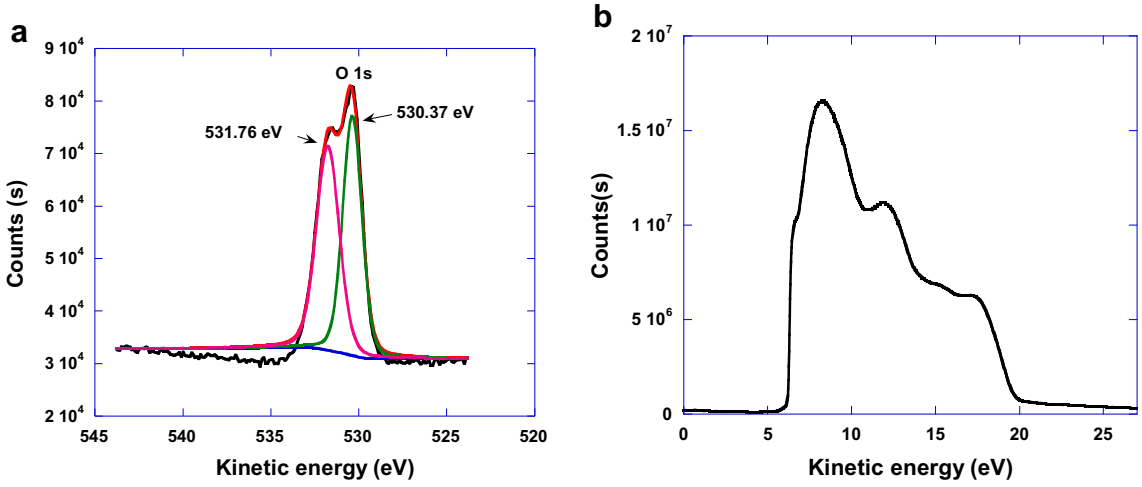

Fig. 4. a) O 1s core-level XPS spectra of the ZnO; b) UPS of the ZnO thin film taken with a −3.0 V bias applied to the sample.

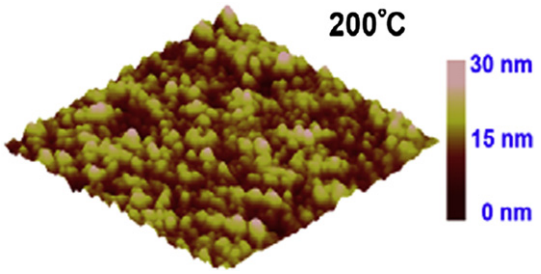

Fig. 5. Surface morphology of ZnO thin films following annealed at 200 °C, observed by tapping mode atomic force microscopy with scan of 1 μm × 1 μm.

for the ZnO thin film annealed at 200 °C. This indicated that the electron transporting property of this ZnO composite layer is not as good as that of bulk ZnO layer. However, such electron mobility is compatible to the electron mobility from most of organic materials used as the electron transporting layer in organic electronics [40]. More important, the low-temperature treatment can be potentially used for making PSCs on plastic substrates because it requires a low-temperature treatment [41]. Therefore, we have chosen ZnO thin films with thermally annealed at 200 °C as a buffer layer for fabrication inverted PSCs.

2.2. Inverted BHJ PSCs

2.2.1. BHJ composite

PSiF-DBT and PCBM are poly[(2,7-dioctylsilafluorene)-2,7-diyl-alt-(4,7-bis(2-thienyl)-2,1,3-benzothiadiazole)-5,5′-diyl]) [42] and [6,6]-phenyl C_{61}-butyric acid methyl ester, respectively. The molecular structures of PSiF-DBT and PCBM are shown in Scheme 1. PSiF-DBT with PCBM together with a ratio of 1.0:2.0 (by weight) was dissolved into o-xylene with a concentration of 20 mg mL^{-1}; continuously stirred above solution at room temperature for 24 h for fabrication polymer solar cells.

2.2.2. Inverted PSCs fabrication

PSCs with an inverted device structure were fabricated by following steps. Approximately 100 nm PSiF-DBT:PCBM layer was deposited by spin-coating PSiF-DBT:PCBM solution onto top of ZnO thin films. The pre-devices were pumped down in the vacuum ($\sim 2 \times 10^{-4}$ Pa). A ~4 nm thickness of molybdenum oxide (MoO_3) was thermally deposited onto the top of PSiF-DBT:PCBM layer at an evaporation rate of 0.1 Às^{-1}. Ultimately, a ~50 nm Au film was deposited on the top of MoO_3 layer through shade mask. The active layer of the device was 0.16 cm^2. All the devices were encapsulated with resin then exposured to ultraviolet light for 3 min and thermally heated at 60 °C for 30 min before characterization.

2.2.3. Inverted PSCs characterization

PCEs were measured under an illumination of 80 m W cm^{-2} with an AM 1.5 solar simulator (Oriel model 91192). For PSCs with ZnO buffer layer, the light intensity was 72 m W cm^{-2} since UV light was blocked by ZnO thin layer (see Fig. 1). The current density-voltage (J–V) characteristics were measured with a Keithley 240 source-measure unit.

2.2.4. Performance of inverted PSCs

The device architectures under our investigation are: ITO/ZnO/PSiF-DBT:PCBM/MoO_3/Au (Device A) and ITO/PSiF-DBT:PCBM/MoO_3/Au (Device B). Scheme 2 depicts the energy diagrams of ITO, ZnO, PSiF-DBT, PCBM, and Au. The current density-voltage (J–V) characteristics of PSCs were shown in Fig. 8. PSCs with ZnO buffer layer show J_{sc} of 5.03 mA cm^{-2}, V_{oc} of 0.90 V and FF of 0.60, resulting in PCEs of 3.8%; PSCs without ZnO buffer layer, only show J_{sc} of 4.23 mA cm^{-2}, V_{oc} of 0.81 V, FF of 0.39, resulting in PCEs of 1.67%. The PCEs observed from PSCs with ZnO buffer layer is more than two times larger than that observed from PSCs without ZnO buffer layer. Therefore, ZnO buffer layer plays an important role in enhancement of PCEs for inverted PSCs.

Table 1 summarized the performance characteristics of inverted PSCs with and without ZnO buffer layer. It was found that inverted PSCs have significant improvements in FF (from 0.39 to 0.60) and V_{oc} (from 0.81 V to 0.90 V) by introduction of ZnO buffer layer. This indicated that ZnO efficiently suppresses the leakage current at the organic/ITO interface, originated from smooth ZnO surface (see Fig. 5).

Considering the devices without ZnO, both PSiF-DBT and PCBM are directly in contact with ITO. It is possible for hole to transfer from PSiF-DBT to ITO, thereby increasing the leakage currents. As shown in Scheme 2, the HOMO (highest occupied molecular orbital) of ZnO (−7.6 eV) is lower than the HOMO of PSiF-DBT (−5.4 eV), showing that ZnO can block the reverse hole flow from PSiF-DBT to ITO. Thereby, ZnO can effectively prevent the leakage current at the organic/ITO interface. In addition, the LUMO (lowest

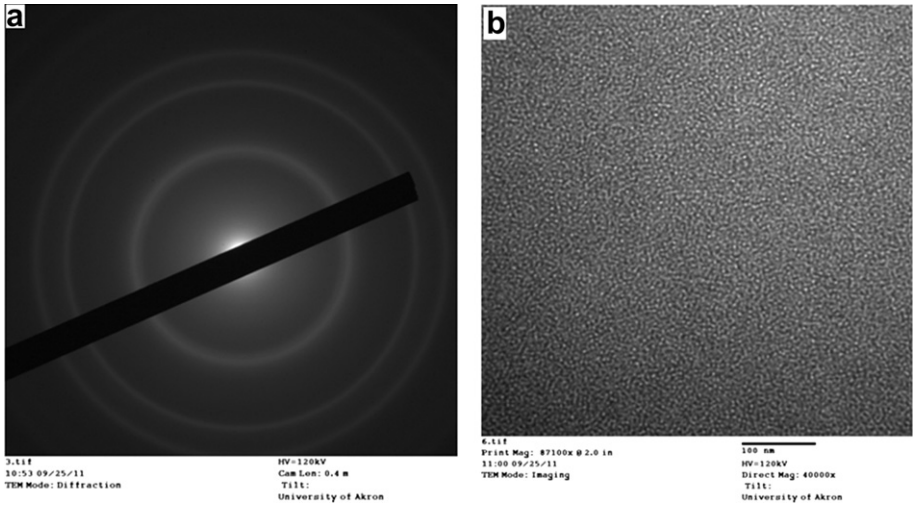

Fig. 6. TEM images of the solution-processed ZnO annealed at 200 °C, a) diffraction mode, b) imaging mode.

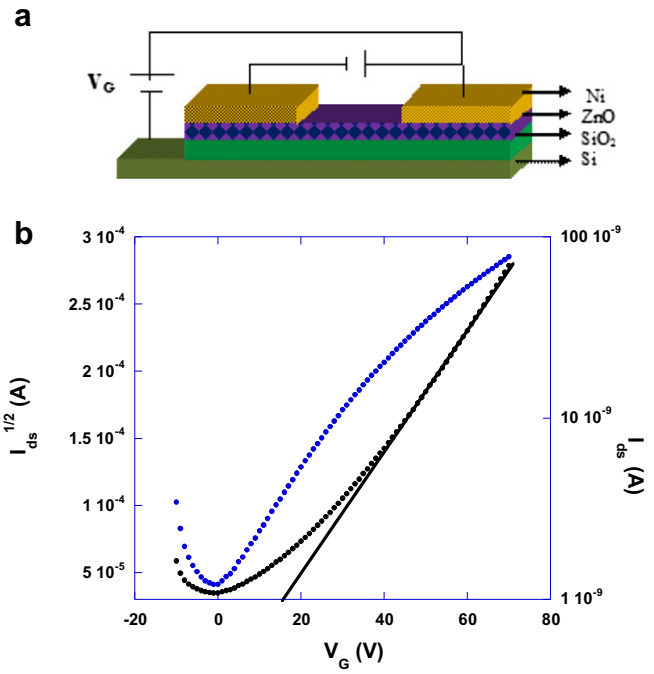

Fig. 7. TFT characteristics used a solution-processed ZnO thin film annealed 200 °C as an active layer. a) Device structure, b) Transfer characteristics.

unoccupied molecular orbital) of ZnO (−4.4 eV) is close to the LUMO of PCBM, revealing that ZnO will help collecting electrons.

Based upon the equivalent circuit of and the current density versus voltage characteristics of photovoltaic cells, solar cells must have small series resistance, R_S, and larger shunt resistance, R_{SH}, for obtaining high short-circuit current, J_{sc} [43,44] As shown in Table 1, the increase in J_{sc} from Device B to Device A, implies significant decrease in R_S, and increase in R_{SH}. From numerical analysis [43–45], we found that R_S decreased from R_S = 56 Ω cm^2 to R_S = 13 Ω cm^2; R_{SH} increased from R_{SH} = 600 Ω cm^2 to R_{SH} = 1400 Ω cm^2 from Device B to Device A, respectively.

Fig. 9 shows the current density vs. voltage characteristics of inverted PSCs measured without illumination. It is also known that the high R_{SH} indicates less leakage current across the solar cells [46]. The current density at reversed biases from Device A is approximately two orders of magnitudes smaller than that from Device B. The low leakage current and elevated R_{SH} are strong evidence showing that the ZnO layer can serve as both an electron-transporting layer and a hole-blocking layer to effectively prevent the leakage currents, resulting in the dramatic improvement in PCEs.

We have further investigated both operation and shelf stabilities of inverted PSCs with and without ZnO buffer layer. The operational

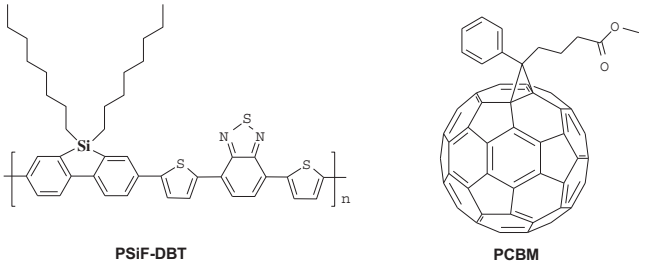

Scheme 1. Molecular structures of PSiF-DBT and PCBM.

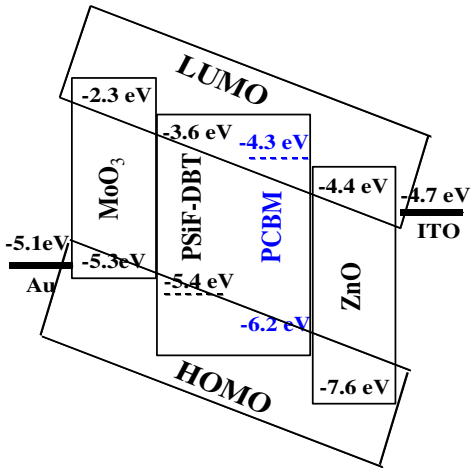

Scheme 2. Energy diagram of PSiF-DBT, PCBM, MoO_3, ZnO, Au and ITO.

stabilities of inverted PSCs with and without ZnO buffer layer were shown in Fig. 10a. Inverted PSCs with ZnO buffer layer did not show obviously degradations in J_{sc}, V_{oc} and FF after continuously illuminating the devices for 4 h. However, for the inverted PSCs without ZnO buffer layer, significant degradations in V_{oc}, FF and J_{sc} were observed after continuously illuminating the devices only for 1 h. All these results indicate that inverted PSCs by using ZnO as the buffer layer have a good operational stability, and the inverted PSCs without ZnO buffer layer are unstable under the illumination condition.

A good operational stability of inverted PSCs with ZnO buffer layer is probably originated from the ZnO block the UV light (see Fig. 1) resulting in a negligible UV light induced photodegradation of organic materials. A significant degradation observed from inverted PSCs without ZnO buffer layer is attributed to the UV light induced photodegradation because UV light directly shining the organic layer through ITO electrode.

Figs. 10b and c show the shelf lifetimes of inverted PSCs with ZnO buffer layer. No obviously degradations in J_{sc}, V_{oc}, FF and PCEs are observed after the devices stored in glove-box for 47 days. Only 5% degradation in PCEs was observed from the devices after 47 days as compared with the fresh devices. We further continually

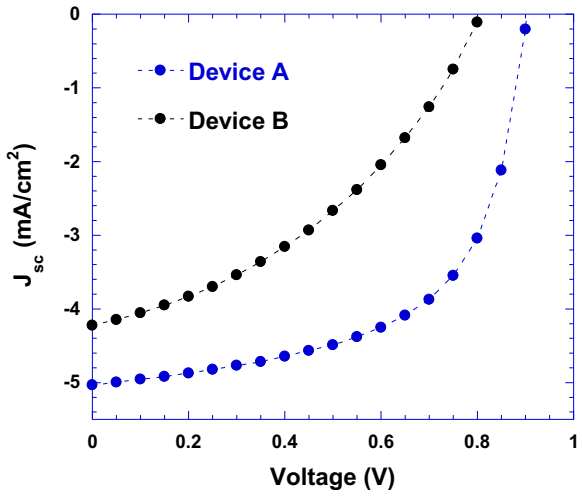

Fig. 8. J–V characteristics of PSCs with the structures of ITO/ZnO/PSiF-DBT:PCBM/MoO_3/Au (Device A) and ITO/PSiF-DBT:PCBM/MoO_3/Au (Device B).

Table 1
Summarized performance characteristics of inverted polymer solar cells.

Device	Active layer	J_{sc} (mA/cm^2)	V_{oc} (V)	FF (%)	PCEs (%)
A	PSiF-DBT:PCBM	5.03	0.90	0.60	3.80
B	PSiF-DBT:PCBM	4.23	0.81	0.39	1.67

Device A: ITO/ZnO/PSiF-DBT:PCBM/MoO_3/Au.
Device B: ITO/PSiF-DBT:PCBM/MoO_3/Au.

investigated the shelf stability of inverted PSCs. Fig. 10d shows the shelf stability of devices after 160 days. Only 10% degradation in PCEs was observed from the devices after 160 days as compared with the fresh devices. All these results demonstrated that inverted PSCs by using ZnO as a buffer layer have very good shelf stability.

2.3. Conclusion

Solution-processed ZnO thin film as a buffer layer for inverted PSCs has been demonstrated. PCEs of 3.8% was observed from inverted PSCs with a device structure of ITO/ZnO/PSiF-DBT:PCBM/MoO_3/Au. Without ZnO layer, PSCs only show PCEs of 1.67%, which is less than half value observed from inverted PSCs with ZnO buffer layer. We also found that inverted PSCs with ZnO buffer layer have both good operation and shelf stabilities. Operated at room temperature, there is no obviously degradation observed from the inverted PSCs with ZnO layer after continuously illuminating the devices for 4 h. There is only 10% degradation observed in PCEs after 160 days. All these results demonstrate that inverted PSCs by using ZnO as the buffer layer have high PCEs and good stabilities.

3. Interfacial engineering via conjugated polyelectrolyte for high performance inverted polymer solar cells

3.1. Preparation of ZnO thin film and ZnO/PFN-Br thin film

ZnO thin film was prepared by the method described above. The ZnO/PFN-Br thin film was prepared by deposition ~5 nm thick of PFN-Br from PFN-Br water-alcohol (1:1 by volume) solution on the top of ZnO thin film.

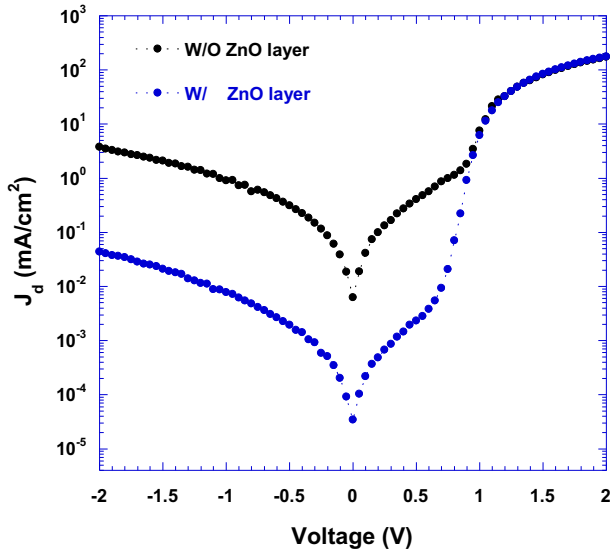

Fig. 9. The current density–voltage characteristics of inverted PSCs with and without ZnO buffer layer measured without light illumination.

3.2. Characterization of ZnO and ZnO/PFN-Br thin films

3.2.1. Absorption spectra

the absorption spectra of solid thin film, ZnO and ZnO/PFN-Br were measured by an HP 8453 UV–vis spectrophotometer. Fig. 11 show the absorption spectrum of ZnO and ZnO/PFN-Br thin films. The ZnO/PFN-Br thin film only absorbs UV light and is transparency from 400 nm to 1000 nm which is similar to the absorption spectrum of ZnO thin film. This indicated that the visible light is allowed to pass through ZnO/PFN-Br thin layer into BHJ composite active layer. Therefore, the photodegradation of polymer active layer is reduced; as a result, a good stability from inverted PSCs is anticipated [19].

3.2.2. Energy levels

In order to verify the effect of PFN-Br on ZnO thin layer, UPS was carried out to study the energy levels of ZnO thin layer and ZnO/PFN-Br thin layer. The UPS measurements were carried out in a Thermo Fisher Scientific Ultra Spectrometer (ESCALAB 250) using He I (21.22 eV) discharge lamp. A bias of −5.0 V was applied to the samples for separation of the sample and the secondary edge for the analyzer.

The low kinetic energy cutoff (E_{cutoff}) of ZnO and ZnO/PFN-Br thin layers were shown in Fig. 12a. E_{cutoff} was estimated by linear extrapolation of the low secondary electrons portion of the spectrum and finding the interset with the background signal [47]. From Fig. 12a, the E_{cutoff} of ZnO and ZnO/PFN-Br were −8.83 eV and −8.57 eV, respectively. There was about −0.26 eV energy difference between ZnO/PFN-Br thin layer and ZnO thin layer. This difference indicated that a dipole was formed [48,49] between PFN-Br layer and ZnO layer.

The highest occupied molecular obtial (HOMO) energy levels for ZnO and ZnO/PFN-Br thin layers were shown in Fig. 12b. The HOMO energies are determined by

$$E_{HOMO} = hv - \left(E_{onset}^{HOMO} - E_{cutoff}\right)^{48} \quad (3)$$

where hv is the incident photon energy, hv = 21.22 eV; E_{cutoff} is defined as the lowest kinetic energy of the measured electrons which can be obtained from Fig. 12a; E_{onset}^{HOMO}. The HOMO energy onset, generally referred to the high kinetic energy onset. From Fig. 12b, the E_{onset}^{HOMO}. r ZnO was 22.4 eV, and the E_{onset}^{HOMO}. r ZnO/PFN-Br was 22.9 eV. Thus, the HOMO energies for ZnO and PFN-Br/ZnO are −7.65 eV and −6.89 eV, respectively. Based on these HOMO energies and optical gaps obtained from the onset of absorption spectra (Fig. 11), the estimated LUMO energy levels were −4.46 eV for ZnO thin layer and −4.08 eV for ZnO/PFN-Br thin layer, respectively. The difference in LUMO energy levels between ZnO and ZnO/PFN-Br indicated that the LUMO energy levels of ZnO was tuned by PFN-Br thin layer. More importantly, this energy difference implied that the band alignment in the inverted PSCs with and without PFN-Br interficial layer is different [50–52]. Therefore, a large V_{oc} from the inverted PSCs with PFN-Br interfical layer is anticipated.

3.2.3. Electronic conductivities

the electronic conductivities of ZnO and ZnO/PFN-Br thin films were conducted on Bruker Dimension Icon system with Peak Force Tapping Tunneling AFM (PFTUNA) module. The probe was the PFTUNA probe with spring constant of ~0.5 N/m with 20 nm Pt/Ir coating on both front and back side. The spring was constantly measured using thermal tune method. The peak currents were measured with bias voltage applied to the sample. The ramp rate of 0.4 Hz and the force setpoint of ~60 nN were for both thin films.

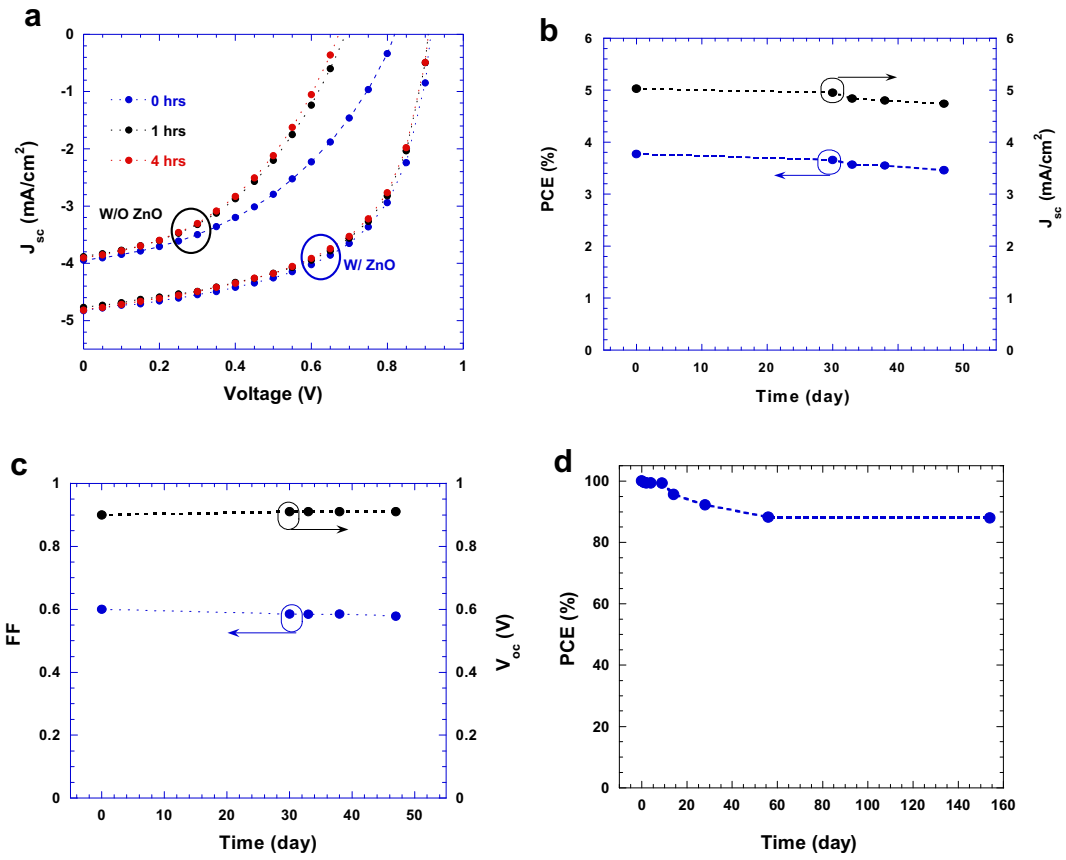

Fig. 10. Stability of PSCs with and without ZnO layer, (a) operation lifetime, (b), (c) and (d) shelf lifetimes.

PFTUNA module was used to measure the peak currents with bias voltage applied to the ZnO and ZnO/PFN-Br thin layers [16]. The peak currents were shown in Fig. 13a and b. the maximum peak current observed from pristine ZnO thin layer is about 5 pA within a 7 μm zoom, however, the maximum peak current observed from ZnO/PFN-Br thin layer is about 25 pA within a 4 μm zoom. These qualitative studies indicated that the electronic conductivity of ZnO/PFN-Br thin layer is much higher than that of ZnO thin layer. This high electronic conductivity will facilitated electron transport from BHJ composite to corresponding electrode [35,53]. Therefore, higher J_{sc} was observed from the inverted PSCs with PFN-Br interfacial layer rather than that without PFN-Br interfacial layer.

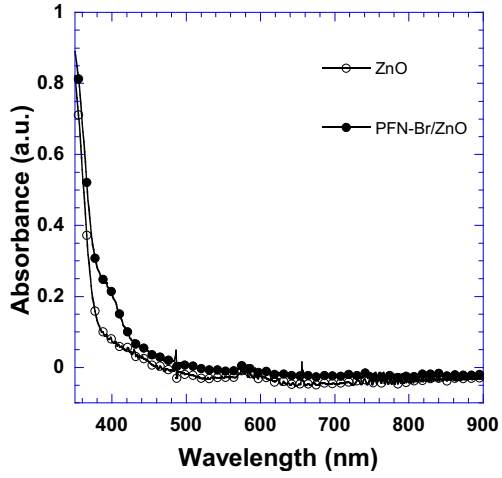

Fig. 11. Absorption spectra of ZnO and Zno/PFN-Br thin films.

3.3. BHJ composite

The BHJ materials under this study are a D–A conjugated polymer, PBDT-DTNT [54] and $PC_{71}BM$. The molecular structures of PBDT-DTNT, $PC_{71}BM$ and PFN-Br [55] are shown in Scheme 3. The synthesis and characterization of PBDT-DTNT and PFN-Br in details were reported elsewhere [54,55]. The $PC_{71}BM$ was purchased from One-Material Inc. and used without further purification. Fig. 14 shows the absorption spectra of PBDT-DTNT, $PC_{71}BM$, BHJ composite of PBDT-DTNT:$PC_{71}BM$ and ZnO/PFN-Br thin films. The bandgap of PBDT-DTNT is 1.48 eV, which is closer to the ideal bandgap for PSCs donor materials [56]. The is the reason that we selected PBDT-DTNT rather than PSiF-DBT as the electron donor for approaching high performance inverted PSCs. PBDT-DTNT has absorption from 400 nm to 800 nm $PC_{71}BM$ has absorption from 400 nm to 700 nm. The absorption spectrum of PBDT-DTNT:$PC_{71}BM$ BHJ composite is the super positions of PBDT-DTNT and $PC_{71}BM$ which implies that both PBDT-DTNT and $PC_{71}BM$ will contribute photocurrent for PSCs fabricated by PBDT-DTNT:$PC_{71}BM$.

3.4. Inverted PSCs fabrication

Two types of inverted PSCs were fabricated on ITO-coated glass substrates. For the inverted PSCs with ZnO thin layer as an electron extraction layer, an approximately 40 nm ZnO thin film was deposited on the top of ITO glass using the method described in the

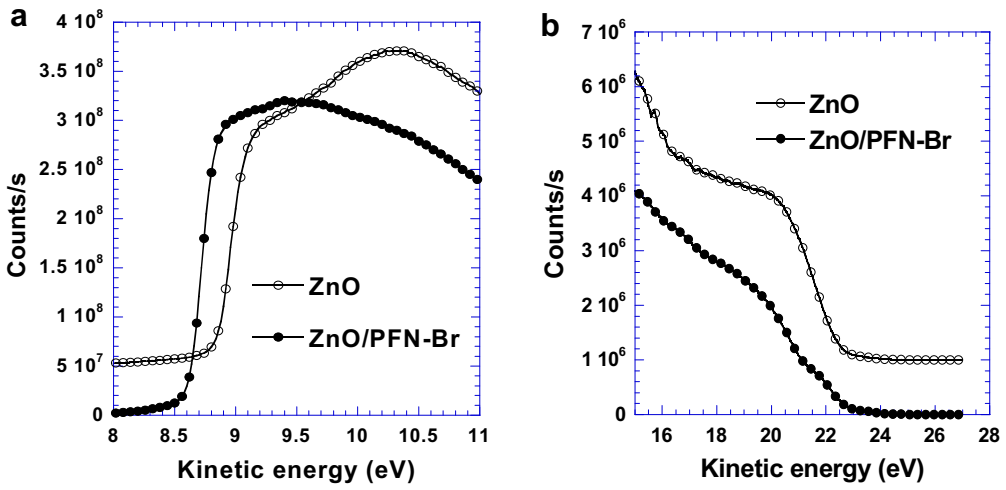

Fig. 12. UPS spectra of (a) the inelastic cutoff region and (b) the HOMO region of ZnO and ZnO/PFN-Br thin layers.

Section 2.1.1. For the inverted PSCs with ZnO/PFN-Br as an electron extraction layer, an approximately 5 nm thick PFN-Br layer was casted on the top of ~40 nm thick ZnO which was coated on the ITO glass. Photoactive layer PBDT-DTNT:$PC_{71}BM$ BHJ composite with an approximately 250 nm thick was then spin coated on either ZnO or ZnO/PFN-Br layer from 1,2-dichlorobenzene solution composed of PBDT-DTNT and $PC_{71}BM$ (PBDT-DTNT:$PC_{71}BM$ = 1:1.5, by weight). The photoactive layer was then thermally annealed at 110 °C for 10 min. After that, about 8 nm molybdenum oxide (MoO_3) was thermally deposited on the top of PBDT-DTNT:$PC_{71}BM$ layer with an evaporation rate of 0.1 Å s^{-1} under the vacuum of ~3 × 10^{-4} Pa. Ultimately, about 60 nm Ag film was deposited on the top of MoO_3 layer through a shade mask. The device area was 0.16 cm^2. All the devices were encapsulated with resin and exposed to ultraviolet light for 5 min in the glove-box with nitrogen atmosphere before testing in air. Scheme 4 shows the device architecture of inverted polymer solar cells with PFN-Br interfacial layer.

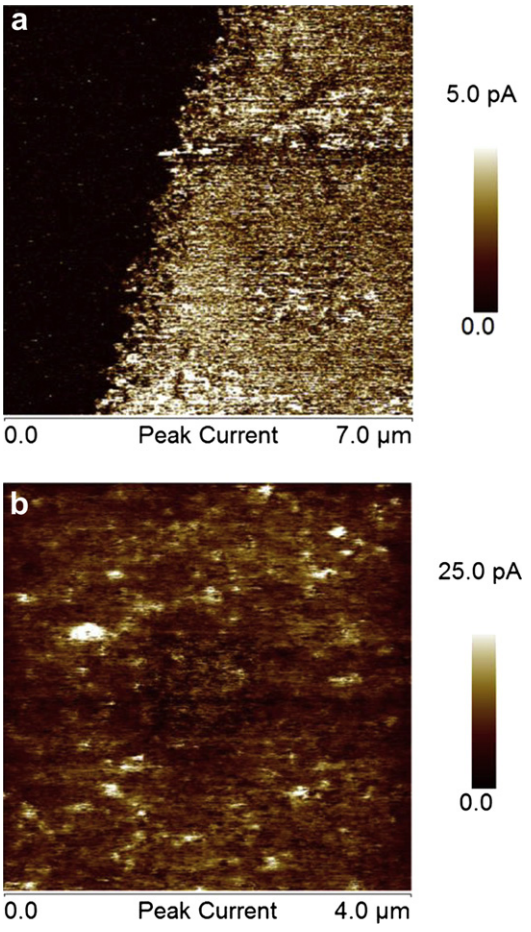

Fig. 13. The peak currents of ZnO (a) and ZnO/PFN-Br (b) surfaces measured by the peak force tapping tunneling AFM (PFTUNA).

3.5. Characterization of inverted PSCs

The current densities–voltage (J–V) characteristics were measured using a Keithley 2400 Source Measure Unit. The solar cells were characterized using a Newport Air Mass 1.5 Global (AM 1.5G) full spectrum solar simulator with an irradiation intensity of 95 m W cm^{-2}.

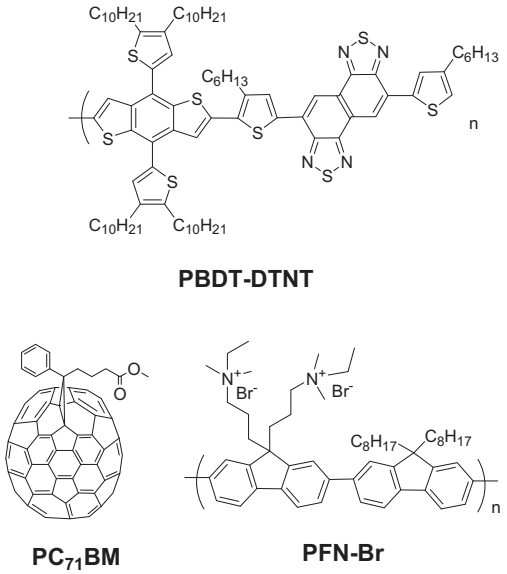

Scheme 3. The molecular structures of PFN-Br, PBDT-DTNT, and $PC_{71}BM$.

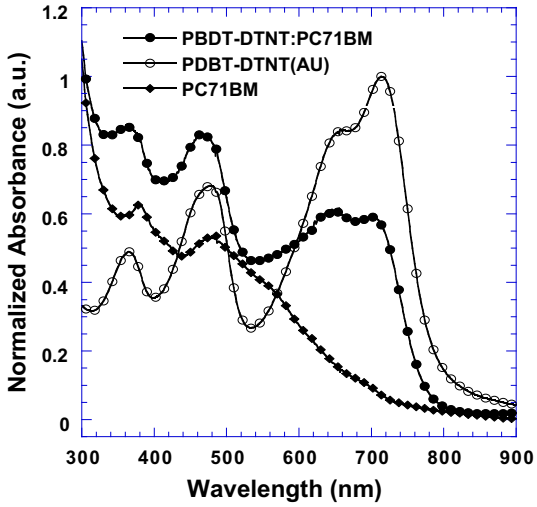

Fig. 14. Absorption spectra of PBDT-DTNT, $PC_{71}BM$ and PBDT-DTNT:$PC_{71}BM$.

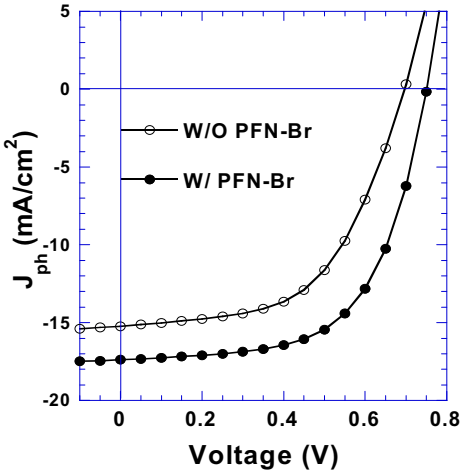

Fig. 15. J versus V characteristics of inverted PSCs with the device architecturs of ITO/ZnO/active layer/Ag and ITO/ZnO/PFN-Br/active layer/Ag under illumination.

The Incident photon-to-current efficiency (IPCE) spectra of inverted PSCs were measured by Solar Cell Quantum Efficiency Measurement System (QEX10) from PV Measurements, Inc.

3.6. Performance of inverted PSCs

Photovoltaic characteristics were investigated for the inverted PSCs with device architectures of ITO/ZnO/PBDT-DTNT:$PC_{71}BM$/MoO_3/Ag and ITO/ZnO/PFN-Br/PBDT-DTNT:$PC_{71}BM$/MoO_3/Ag. J–V characteristics were shown in Fig. 15. Without PFN-Br interfacial layer, inverted PSCs showed a short-circuit current (J_{sc}) of 15.2 mA cm^{-2}, an open-circuit voltage (V_{oc}) of 0.69 V, a fill factor (FF) of 55% and a corresponding PCE of 6.1%. After depositing a thin conjugated polyelectrolyte layer, PFN-Br, onto ZnO thin film to reengineering the interface between ZnO electron extraction layer and PBDT-DTNT:$PC_{71}BM$, inverted PSCs showed a J_{sc} of 17.4 mA cm^{-2}, a V_{oc} of 0.75 V, an FF of 61% and a corresponding PCE of 8.4%. Over 37% enhanced PCEs were observed. Device performance optimization involved over 500 identical devices fabricated from over 100 independently PBDT-DTNT:$PC_{71}BM$, and ZnO/PFN-Br thin films; PCEs between 8.2% and 8.6% were obtained. The average device yields PCE of 8.4%, with J_{sc} of 17.4 mA cm^{-2} (the calculated J_{sc} value from IPCE spectrum was 17.2 mA cm^{-2}). This highest efficiency reported from inverted BHJ PSCs was recorded by the colleagues from the South China University of Technology [57].

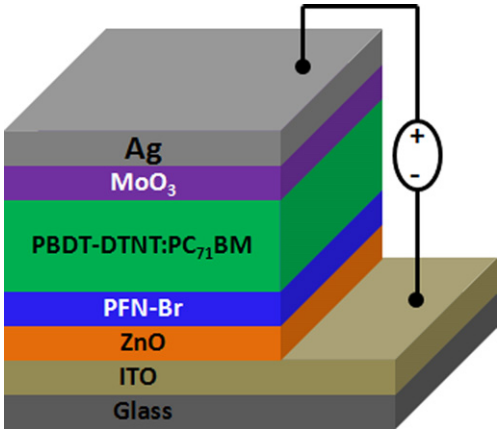

Scheme 4. Architecture of inverted polymer solar cells with PFN-Br interfacial layer.

The V_{oc} of 0.75 V from the inverted PSCs with PFN-Br interfacial layer was larger than V_{oc} of 0.69 V from the inverted PSCs without PFN-Br interfacial layer. This difference was due to the different band alignments in the inverted PSCs with and without PFN-Br interfacial layer. This observation is in good agreement with the band alignment showed in Scheme 5. Scheme 5 shows the band alignment of BHJ composite and two buffer layers with the work function of ITO and Ag electrodes.

Fig. 16 shows the J–V characterisitics of inverted PSCs with and without PFN-Br interfacial layer measured in dark. It was found that the dark current densities under the reverse bias from the inverted PSCs with PFN-Br interfacial layer are approximatlively 10 times smaller than those from the inverted PSCs without PFN-Br interficail layer. The low dark current densities observed from the inverted PSCs with PFN-Br interfacial layer indicated that the bimolecular recombination was suppressed by PFN-Br interfacial layer [53,58,59]. Thus, high photocurrent is expected.

More importantly, the low dark current densities observed from the inverted PSCs with PFN-Br interfacial layer implied that the inverted PSCs with PFN-Br interficail layer possess larger V_{oc} than

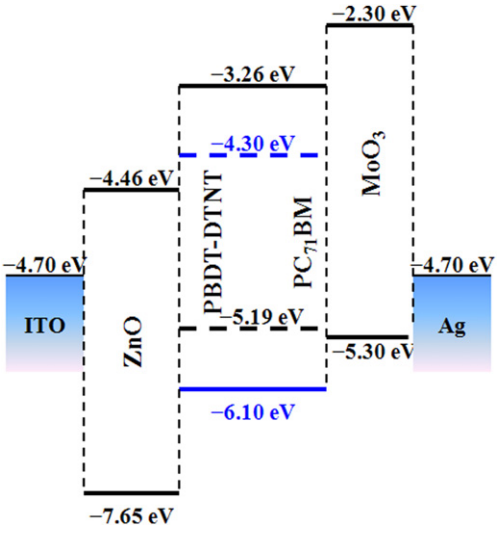

Scheme 5. Energy-level diagram showing the HOMO and LUMO energies of each component material and the work functions of ITO cathode and Ag anode.

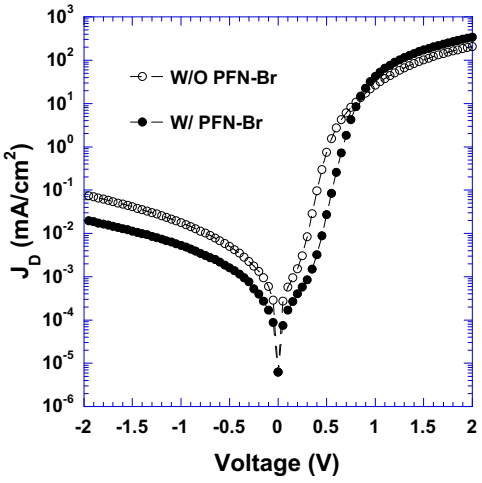

Fig. 16. J versus V characterisitics of inverted PSCs with the device archetecturs of ITO/ZnO/active layer/Ag and ITO/ZnO/PFN-Br/active layer/Ag in dark.

those without PFN-Br interficail layer [53]. Toward the end, we have modeled the J–V characteristics of PSCs with an equivalent circuit, consisting of single diode with series resistance (R_S) and shunt resistance (R_{SH}). The addition of a parallel photocurrent source, J_{ph}, leads to the well-known equation [53].

$$J = J_0\left[\exp\left(\frac{q(V - R_sAJ)}{nkT}\right) - 1\right] + \frac{V - R_sAJ}{R_{sh}A} - J_{ph}(V) \quad (4)$$

where q is the electron charge; k is Boltzmann's constant; T is the temperature; and J_{ph} is the voltage–dependent photocurrent produced by the cell. By rearranging Equ. 3 under open circuit condition ($J = 0$) and $J_{ph} = J_{sc}$, V_{oc} can be described as

$$V_{oc} \approx \frac{nKT}{q}\ln\left(\frac{J_{sc}}{J_0}\right) \quad (5)$$

where J_0 is reverse dark current density. According to Equ (5), lower J_0, higher V_{oc}. Therefore, inverted PSCs with PFN-Br interficail layer possesses a higher V_{oc} than that PSCs without PFN-Br interficail layer.

Device performance parameters were summarized in Table 2. The enhanced J_{sc} and FF in the inverted PSCs with PFN-Br interfacial layer implied that R_S in the inverted PSCs with PFN-Br interfacial layer was smaller than that without PFN-Br interfacial layer, and R_{SH} in the inverted PSCs with PFN-Br interfacial layer is larger than that without PFN-Br interfacial layer. In order to confirm this hypothesis, we have calculated R_S and R_{SH} based on the J–V curves shown in Fig. 3a. The R_S for the inverted PSCs with and without PFN-Br interfacial layer are 6.1 Ω cm^2 and 10.3 Ω cm^2, respectively. The R_{SH} for the inverted PSCs with and without PFN-Br interfacial layer are 757.6 Ω cm^{-2} and 490.2 Ω cm^2, respectively. It is indeed that the R_S in the inverted PSCs with PFN-Br interfacial layer is smaller than that without PFN-Br interfacial layer, and the R_{SH} in the inverted PSCs with PFN-Br interfacial layer is larger than that without PFN-Br interfacial layer.

Table 2
Performance of inverted PSCs with and without PFN-Br.

Device structure	V_{oc} (V)	J_{sc} mA cm^{-2}	FF (%)	R_S Ω cm^2	R_{SH} Ω cm^2	PCE (%)
Device A[a]	0.69	15.2	55	10.3	490.2	6.1
Device B[b]	0.75	17.4	61	6.1	757.6	8.4

[a] ITO/ZnO/PBDT-DTNT: $PC_{71}BM/MoO_3$/Ag.
[b] ITO/ZnO/PFN-Br/PBDT-DTNT: $PC_{71}BM/MoO_3$/Ag.

Fig. 17 compared the IPCE spectra of the inverted PSCs with and without PFN-Br interfacial layer. Inverted PSCs with PFN-Br interfacial layer exhibited a substantial enhanced response from 400 nm to 800 nm as compared with that without PFN-Br interfacial layer. The inverted PSCs with PFN-Br interfacial layer showed a high IPCE response over 64% from 400 nm to 750 nm, with a maximum value of 76% at 550 nm. Compared with the inverted PSCs without PFN-Br interfacial layer, the inverted PSCs with PFN-Br interfacial layer also exhibited a small difference in the spectral from 490 nm to 720 nm. This difference is probably originated from different internal optical electric field distributions due to complex index of refraction and layer thickness of ZnO and ZnO/PFN-Br [60,61]. As shown in Fig. 16, a large forward current observed in the inverted PSCs with PFN-Br interfacial layer rather than that without PFN-Br interfacial layer [59,60]. This indicated the contact between PFN-Br interfacial layer and BHJ composite active layer is better than that between ZnO layer and BHJ composite active layer. Therefore, an enhanced IPCE response was observed from the inverted PSCs with PFN-Br interfacial layer.

AFM was carried out to further investigation of the influence of PFN-Br interfacial layer on the device performance. Fig. 18a and b compared the surface morphologies of pristine ZnO and ZnO/PFN-Br thin films. With scale of 10 μm × 10 μm, the root mean square (RMS) for ZnO/PFN-Br is 2.335 nm, and RMS for ZnO is 1.375 nm. The rough surface offers a better interaction between PBDT-DTNT:$PC_{71}BM$ BHJ composite layer and ZnO electron exaction layer whereas the smooth surface indicated that interfacial adhesion between PBDT-DTNT:$PC_{71}BM$ BHJ composite layer and ZnO electron exaction layer was weak [3,62]. Fig. 18c and d displayed the surface morphologies of PBDT-DTNT:$PC_{71}BM$ on the pristine ZnO thin film and on the ZnO/PFN-Br thin film, respectively. The RMS for PBDT-DTNT:$PC_{71}BM$ on the pristine ZnO thin film and on the PFN-Br/ZnO thin film are 3.353 nm and 5.858 nm, respectively. Different roughness surfaces implied that the interfacial adhesion between MoO_3 hole extraction layer and PBDT-DTNT:$PC_{71}BM$ layer are different. The rougher surface, the better interfacial adhesion is prospected [3,62]. Consequently, a better charge transport is expected from a good interfacial adhesion between MoO_3 hole extraction layer and PBDT-DTNT:$PC_{71}BM$ BHJ layer.

3.7. Conclusions

Through a conventional active-layer processing methodology, efficient BHJ PSCs with the inverted device structure based on

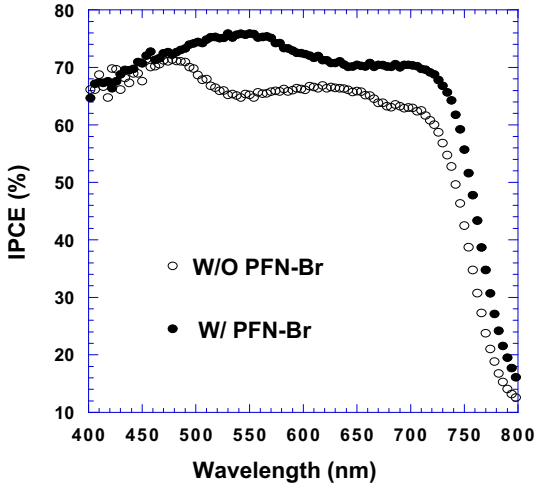

Fig. 17. IPCE (%) versus wavelength for inverted PSCs with the device structures of ITO/ZnO/PBDT-DTNT:$PC_{71}BM/MoO_3$/Ag and ITO/ZnO/PFN-Br/PBDT-DTNT:$PC_{71}BM/MoO_3$/Ag.

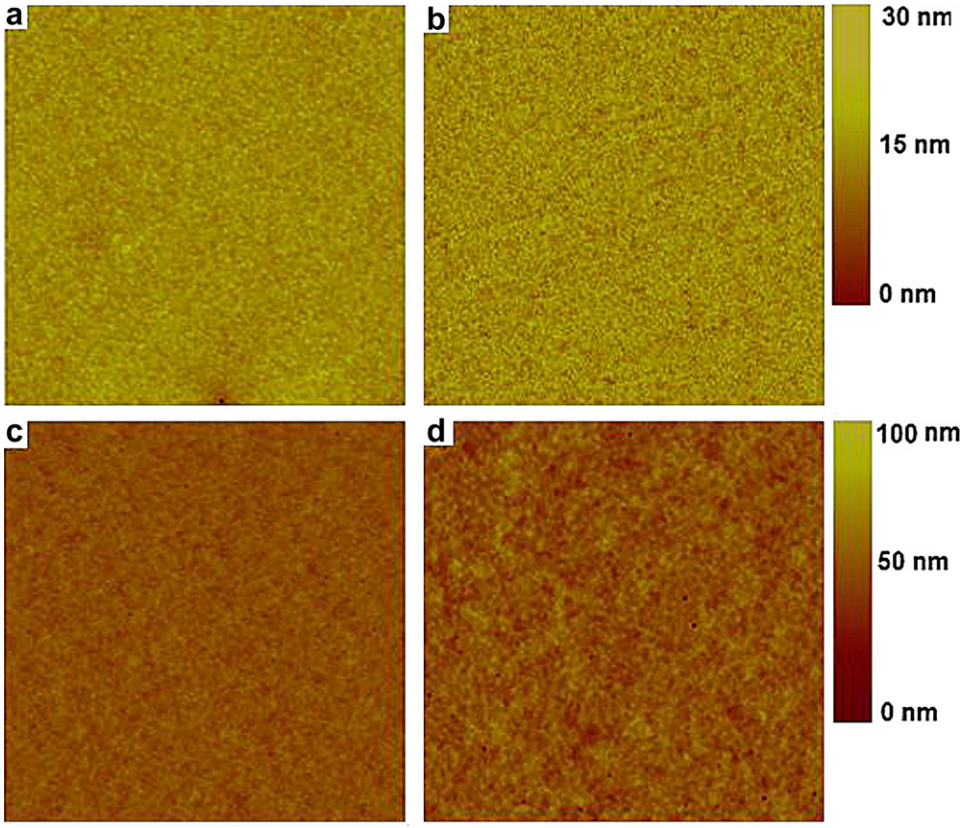

Fig. 18. Tapping-mode AFM images: (a) the surface of pristine ZnO thin film, RMS: 1.375 nm (10 μm × 10 μm), (b) the surface of ZnO/PFN-Br thin film, RMS: 2.335 (10 μm × 10 μm), (c) PBDT-DTNT:PC_{71}BM on the top of pristine ZnO thin film, RMS: 3.353 nm (20 μm × 20 μm), (d) PBDT-DTNT:PC_{71}BM on the top of ZnO/PFN-Br thin film, RMS: 5.858 nm (20 μm × 20 μm).

PBDT-DTNT:PC_{71}BM composites have been fabricated. Power conversion efficiency of 8.4% under AM 1.5 G illumination was achieved from the inverted PSCs by using a PFN-Br interfacial layer to engineering ZnO electron extraction layer. Without PFN-Br interfacial layer, the inverted PSCs only showed an efficiency of 6.1% under the same condition. The overall enhanced short-circuit current density, open-circuit voltage, fill factor and corresponding high efficiency in the inverted PSCs with a thin conjugated polyelectrolyte interfacial layer, were attributed to the good contact between ZnO electron extraction layer and PBDT-DTNT:PC_{71}BM BHJ active layer, good interface adhesion between the electron extraction layer and PBDT-DTNT:PC_{71}BM BHJ active layer, and enhanced charge transport via suppressed bimolecular recombination. These results provided an important progress for solution-processed PSCs, and demonstrated that PSCs with an inverted device structure are comparable with PSCs with the conventional device structure.

4. Summary

Solution-processed ZnO thin film as an electron extraction layer for inverted PSCs has been demonstrated. Operated at room temperature, no obviously degradation was observed from the PSCs with ZnO layer after continuously illuminating the devices for 4 h. However, a significantly degradation was observed from the PSCs without ZnO buffer layer after illuminating the devices only for 1 h. Furthermore, PSCs with ZnO buffer layer also show very good shelf stability; only 10% degradation observed in PCEs after 6 months. We further optimize the performance of inverted PSCs. A high PCE of 8.4% under AM 1.5G irradiation was achieved for BHJ PSCs with an inverted device structure. This high efficiency was obtained through interfacial engineering of solution-processed electron extraction layer, ZnO, leading to facilitate electron transport and suppress bimolecular recombination. All these results provided an important progress for solution-processed PSCs, and demonstrated that PSCs with an inverted device structure are comparable with PSCs with the conventional device structure.

Acknowledgments

The author thanks the University of Akron, 3M Company, and the Joint Research Fund for Overseas Chinese Scholars, the National Science Foundation of China (#50828301) for financial support.

References

[1] Sariciftci NS, Smiloitz L, Heeger AJ, Wudl F. Science 1992;258:1474–6.
[2] Li G, Shrotriya V, Huang J, Yao Y, Moriarty T, Emery K, et al. Nat Mater 2005;4:864–8.
[3] Ma W, Yang CY, Gong X, Lee KH, Heeger A. J Adv Funct Mater 2005;15:1617–22.
[4] Blom PWM, Mihailetchi VD, Koster LJA, Markov DE. Adv Mater 2007;19:1551–66.
[5] Park SH, Roy A, Beaupré S, Cho S, Coates N, Moon JS, et al. Nat Photon 2009;3:297–303.
[6] Li YF. Acc Chem Res 2012;45:723–33.
[7] Huo LJ, Zhang SQ, Guo X, Xu F, Li YF, Hou JH. Angew Chem Int Ed 2011;50:9697–702.
[8] Chen HY, Hou J, Zhang S, Liang Y, Yang S, Yang Y, et al. Nat Photon 2009;3:649–53.
[9] Service RF. Science 2011;332:293.
[10] He C, Zhong C, Huang H, Wong WY, Wu H, Chen L, et al. Adv Mater 2011;23:4636–43.
[11] Dou L, You J, Yang J, Chen C-C, He Y, Murase S, et al. Nat Photon 2012 [online].

[12] de Jong MP, van IJzendoorn LJ, de Voigt MJA. Appl Phys Lett 2000;77:2255–7.
[13] Pacios R, Chatten AJ, Kawano K, Durrant JR, Bradley DDC, Nelson J. Adv Funct Mater 2006;16:2117–26.
[14] Krebs FC, Norrman K. Prog Photovolt Rev Appl 2007;15:697–712.
[15] Jørgensen M, Norman K, Krebs FC. Sol Energy Mater Sol Cells 2008;92:686–714.
[16] Yang TB, Wang M, Cao Y, Huang F, Huang L, Peng JB, et al. Adv Energy Mater 2012;2:523–7.
[17] Sahin Y, Alem A, Bettignies R, Nunzi JM. Thin Solid Films 2005;476:340–3.
[18] Hau SK, Yip HL, Baek NS, Zou J, O'Malley K, Jen AKY. Appl Phys Lett 2008;92:253301–3.
[19] Yang T, Cai W, Qin D, Wang E, Lan L, Gong X, et al. J Phys Chem C 2010;114:6849–53.
[20] Zimmermann B, Würfel U, Niggemann M. Sol Energy Mater Sol Cells 2009;93:491–4.
[21] Sun Y, Takacs CJ, Cowan SR, Seo JH, Gong X, Roy R, et al. Adv Mater 2011;23:2226–30.
[22] Zeng W, Wu H, Zhang C, Huang F, Peng J, Yang W, et al. Adv Mater 2007;19:810–4.
[23] Waldauf C, Morana M, Denk P, Schilinsky P, Coakley K, Choulis SA, et al. Appl Phys Lett 2006;89:233517–9.
[24] Hayakawa A, Yoshikawa O, Fujieda T, Uehara K, Yoshikawa Y. Appl Phys Lett 2007;90:163517–9.
[25] Hänsel H, Zettl H, Krausch G, Kisselev R, Thelakkat M, Schmidt HW. Adv Mater 2003;15:2056–60.
[26] Kim JY, Kim SH, Lee HK, Lee H, Ma W, Gong X, et al. Adv Mater 2006;18:572–6.
[27] Ong BS, Li CS, Li YN, Wu YL, Loutfy R. J Am Chem Soc 2007;129:2750–1.
[28] Chen LM, Hong Z, Li G, Yang Y. Adv Mater 2009;21:1434–49.
[29] Cheng YJ, Hsieh CH, He Y, Hsu CS, Li Y. J Am Chem Soc 2010;132:17381–3.
[30] Sun Y, Seo JH, Takacs J, Seifter J, Heeger AJ. Adv Mater 2011;23:1679–83.
[31] Small CE, Chen S, Subbiah J, Amb CM, Tsang SW, Reynolds JR, et al. Nat Photon 2012;6:115–20.
[32] Tan Z, Zhang W, Zhang Z, Qian D, Huang Y, Hou J, et al. Adv Mater 2012;24:1476–81.
[33] Choi H, Park JS, Jeong E, Kim G-H, Lee BR, Kim SO, et al. Adv Mater 2011;33:2759–65.
[34] Carbonera R, Po C, Bernardi A, Camaioni N. Energy Environ Sci 2011;4:285–310.
[35] Yip H-L, Jen AK-Y. Energy Environ Sci 2012 [online].
[36] Heo YW, Norton DP, Tien LC, Kwon Y, Kang BS, Ren F, et al. Mater Sci Eng R Rep 2005;R47(1–2):1–47.
[37] Pearton SJ, Norton DP, Heo YW, Steiner T. J Vacuum Sci Technol B Microelectronics Nanometer Structures-Processing, Meas Phenomena 2004;22:932–48.
[38] Park JH, Kang GS, Kwon SI, Lim DG, Choi YJ, Park JG. J Nanosci Nanotechno 2008;8:4658–61.
[39] White MS, Olson DC, Shaheen SE, Kopidakis N, Ginley DS. Appl Phys Lett 2006;89:143517–9.
[40] Nelson J, Kwiatkowski JJ, Kirkpatrick J, Frost JM. Acc Chem Res 2009;11:1768–78.
[41] Crawford GP. Flexible flat panel displays. John Wiley & Sons, Ltd; 2005. P. 12–13.
[42] Wang EG, Wang L, Lan LF, Luo C, Zhuang WL, Peng JB, et al. Appl Phys Lett 2008;92:033307–9.
[43] Nelson J. The Physics of solar cells. Imperial College Press; 2003. p.145–76.
[44] Cai WZ, Gong X, Cao Y. Solar Energy Mater Solar Cells 2010;94:114–27.
[45] Raus HC. Solar cell array design handbook. New York: Van Nostrand Reinhold; 1980. P56.
[46] Moliton A, Nunzi JM. Polym Int 2006;55:583–600.
[47] Gao YL. Mater Sci Eng R 2010;68:39–87.
[48] Hill IG, Kahn A. J Appl Phys 1998;84:5583–6.
[49] Tengstedt C, Osikowicz W, Salaneck WR, Parker ID, Hsu C-H. Appl Phys Lett 2006;88:053502–5.
[50] Luo J, Wu H, He C, Li A, Yang W, Cao Y. Appl Phys Lett 2009;95:043301–3.
[51] He C, Zhong C, Wu H, Yang R, Yang W, Huang F, et al. J Mater Chem 2010;20:2617–22.
[52] Seo JH, Gutacker A, Sun Y, Wu H, Huang F, Cao Y, et al. J Am Chem Soc 2011;133:8416–9.
[53] Sze SM, Ng KK. Physics of semiconductor devices. 3rd ed. John Wiley & Sons, Inc; 2007.
[54] Wang M, Hu X, Li W, Gong X, Huang F, Cao Y. J Am Chem Soc 2011;133:9638–41.
[55] Huang F, Wu H, Wang D, Yang W, Cao Y. Chem Mater 2004;16:708–16.
[56] Scharber MC, Mühlbacher D, Koppe M, Denk P, Waldauf C, Heeger AJ, et al. Adv Mater 2006;18:789–94.
[57] He CZ, Zhong CM, Su SJ, Xu M, Wu HB, Cao Y, et al. Nat Photo 2012 [online].
[58] Sarah SR, Roy R, Heeger AJ. Phys Rev B 2010;82:245207. 1–10.
[59] Gong X, Tong MH, Brunetti FG, Seo J, Sun YM, Moses D, et al. Adv Mater 2011;23:2272–7.
[60] Pettersson LAA, Roman LS, Inganäs O. J Appl Phys 1999;86:487–96.
[61] Xue J, Uchida S, Rand BP, Forrest SR. Appl Phys Lett 2004;85:5757–9.
[62] Sekine N, Chou CH, Kwan WL, Yang Y. Org Electronics 2009;10:1473–7.

Xiong Gong, Ph.D. is an Assistant Professor, currently, in the Department of Polymer Engineering at the College of Polymer Science and Polymer Engineering, The University of Akron. He is also Adjunct Professor in the State Key Laboratory of Luminescence Materials and Devices at the South China University of Technology, PR China. Prior to that, he was a senior research scientist in the Center for Polymers and Organic Solids at the University of California, Santa Barbara (UCSB), and a manager and senior scientist at the Cbrite Inc. from 2005 to 2010. He did his postdoctoral fellow with Professor Alan J Heeger (Noble Prize Winner) at UCSB. He obtained his Ph. D. in Physics from Nankai University, M.S. in Chemistry from Lanzhou University and B. S. in Chemistry from Northwest Normal University. He has accomplished 138 articles published in the peer reviewed journals including in Science, with a peer citation over 6000 times. He earned an H-index of 36. He also contributed 29 granted/pending patents and 8 book chapters.